

Physical and Electrochemical Properties of Supercapacitor Electrodes Derived from Carbon Nanotube and Biomass Carbon

R. Farma^{1,2}, M. Deraman^{1,*}, Awitdrus^{1,2}, I.A. Talib¹, R. Omar¹, J.G. Manjunatha,¹M.M. Ishak¹, N.H. Basri¹ and B.N.M. Dolah¹

¹ School of Applied Physics, Faculty of Science and Technology, Universiti Kebangsaan Malaysia, 43600 Bangi, Selangor, Malaysia

² Department of Physics, Faculty of Mathematics and Natural Sciences, University of Riau, 28293 Pekanbaru, Riau, Indonesia

*E-mail: madra@ukm.my

Received: 29 October 2012 / Accepted: 29 November 2012 / Published: 1 January 2013

Green monoliths (GMs) were prepared from mixtures of KOH (5% by weight), carbon nanotubes (5%) and self-adhesive carbon grains (90%) from oil palm empty fruit bunch fibers. The GMs were carbonized up to 600, 700 and 800°C under an N₂ gas environment, and activated by CO₂ gas at 800°C for one hour to produce activated carbon monoliths (ACMs), designated as ACM6, ACM7 and ACM8, respectively. The characterization of the ACMs showed a notable effect of the carbonization temperature on the structure, microstructure, electrical conductivity and porosity of the ACMs. Consequently, three independent methods, galvanostatic charge-discharge, cyclic voltammetry and electrochemical impedance spectroscopy, used for the electrochemical characterization of supercapacitor cells fabricated using the ACMs as their electrodes, consistently found that the ACM7 and ACM8 cells have higher specific capacitance (77 Fg⁻¹ and 85 Fg⁻¹, respectively), specific energy (2.2 Wh kg⁻¹ and 2.1 Wh kg⁻¹, respectively) and specific power (156 W kg⁻¹ and 161 W kg⁻¹, respectively) compared to the ACM6 cell. These results suggest that carbonization should be performed at temperatures closer or equal to the activation temperature for the preparation of supercapacitor electrodes composed of biomass precursors.

Keywords: Self-adhesive carbon grains, Activated carbon monolith, Carbon nanotube, Porosity, Supercapacitor electrode

1. INTRODUCTION

Supercapacitors are electrochemical storage devices whose range of energy and power densities can complement the function of batteries and conventional capacitors for storing energy and delivering

power [1]. The most common types of supercapacitor electrodes include activated carbon (AC), and the carbon-based supercapacitor is widely developed because of its low cost, large capacitance and long cycling life [2]. The electrostatic charges stored at the AC electrode/electrolyte double layer interface produce a high capacitance because of the high specific surface area of the AC electrodes. However, a relatively low electronic conductivity of the AC results in the supercapacitor having a high equivalent series resistance (ESR) and hence lower specific energy (E) and power (P) during charge and discharge. This shortcoming can be resolved by mixing AC with carbon nanotubes (CNTs), which have a higher electronic conductivity [3,4]. Because the CNTs have a lower specific capacitance (C_{sp}) than the AC, the mixture was subjected to physical/chemical activation in an attempt to increase the surface area and specific capacitance (C_{sp}) of the electrode [4,5].

Here, the preparation and characterization of binderless AC monolith (ACM) electrodes from the mixture of self-adhesive carbon grains (SACG) from oil palm empty fruit bunch (EFB) fibers, CNTs and potassium hydroxide (KOH) is reported. KOH is a typical alkaline metal compound that is widely used for the chemical activation of coal precursors, chars and petroleum coke. It has been reported that the chemical reactions between hydroxides (KOH or NaOH) and carbon during the activation process play an important role in the porosity development of the activated carbon [6]. Green monoliths (GMs) of the aforementioned mixtures were carbonized in a N_2 environment up to various carbonization temperatures to produce carbon monoliths (CMs) prior to the CO_2 activation process used to produce the ACMs. The physical activation is usually carried out by treating the carbonized sample within an oxidizing gas atmosphere (such as CO_2 and water vapor) under a moderately high temperature (800-100°C) to improve the internal porosity [7].

In the present study, a new procedure for preparing electrodes by varying the carbonization temperature during the preparation of ACMs from CNTs and AC from EFB fibers based on a combination of chemical (KOH) and physical activation agent (CO_2) is examined. The combination of chemical and physical activation methods has been reported for carbon electrodes from other types of biomass precursors, for example, coffee endocarp [8] and sun flower seed shell [9] precursors. The ACMs were characterized by investigating their density, electrical conductivity, porosity, microstructure and structure with respect to carbonization temperature. The electrochemical behaviors of the supercapacitor cells fabricated using these ACM electrodes were investigated using three different electrochemical characterization techniques. Recent related work has been reported by our research group in references [10-12].

2. EXPERIMENTAL

2.1 Electrode preparation and cell fabrication

SACGs with an average particle size less than 106 μm were prepared from EFB fibers by pre-carbonization (Furnace CTMSB46), milling for 36 hours (ball mill AC Motor BS 500-110) and sieving (Matest 24030 Brembate Sopra (BG)). The mixture was prepared by pouring 27.0 g SACG and 1.5 g of KOH (5% by weight) and CNT (5% by weight) into 300 ml boiling water; the mixture was stirred

for 1 hour and then dried in an oven at 100°C for 48 hour. Approximately 10 g of the dried mixture was milled for 20 min to obtain a homogeneous composition. Following this step, 0.75 g of the mixture was placed inside a mold with a diameter of 20 mm and converted into a GM using a press pelletizing machine (VISITEC 2009-Malaysia).

The GMs were carbonized into CMs in a carbonization furnace (Vulcan Box Furnace 3-1750) under a 1.5 L min⁻¹ flow of N₂ gas, up to 600, 700 and 800°C using our previous multi-step heating profile [13] to produce CM6, CM7 and CM8, respectively. ACM6, ACM7 and ACM8 were produced from these respective CMs via CO₂ (1.0 L min⁻¹) activation at 800°C for 1 hour with a heating rate of 5°C min⁻¹. After being polished to a thickness of 0.4 mm, the ACMs were used as electrodes in symmetrical supercapacitor cells using 316L stainless steel (0.02 mm thick) as current collector, 1 M H₂SO₄ as electrolyte and a Teflon ring as separator (0.1 mm thick).

2.2 Physical and electrical characterizations

The dimensions (Mitutoyo 193-253) and masses (Mettler Toledo AB204) of the monoliths were measured to determine the density of the GMs, CMs and ACMs. The four-point-probe technique (Jandel Universal Probe & Keithley Micro-Ohmmeter 220) was used to determine the electrical conductivity of the ACMs. A field emission scanning electron microscope (FESEM) (Zeiss SUPRA 55VP) was used to study the microstructures of the ACMs. An X-ray diffractometer (Bruker AXS: model D8 Advance, wavelength of 1.5406 Å) was used to record the X-ray diffraction (XRD) patterns of the ACMs. The liquid nitrogen (77 K) adsorption-desorption isotherm experiments (Micromeretic ASAP 2010) were conducted to characterize the porosity of the ACMs.

2.3 Electrochemical characterization

The performance of the supercapacitor cells using ACMs as their electrodes was studied by electrochemical impedance spectroscopy (EIS), cyclic voltammetry (CV) and galvanostatic charge-discharge (GCD) methods using an electrochemical instrument-interface (Solartron SI 1286 and Solartron 1255HF Frequency Response Analyzer). All of the measurements were carried out at room temperature (25°C). Using the EIS data, the C_{sp} of the electrodes was determined using the equation (1):

$$C_{sp} = -\frac{1}{\pi f_l Z_l'' m} \quad (1)$$

where f_l is the lowest frequency, Z_l'' is the imaginary impedance at f_l and m is the weight of electrode.

The EIS data as a function of the frequency were analyzed using equations (2), (3) and (4):

$$C(\omega) = C'(\omega) - jC''(\omega) \quad (2)$$

$$C''(\omega) = Z'(\omega) / \omega |Z(\omega)|^2 \quad (3)$$

$$C'(\omega) = -Z''(\omega) / \omega |Z(\omega)|^2 \quad (4)$$

where $Z(\omega)$ is equal to $1/j\omega C(\omega)$, $C'(\omega)$ is the real capacitance, $C''(\omega)$ is the imaginary capacitance, $Z'(\omega)$ is the real impedance and $Z''(\omega)$ is the imaginary impedance [14].

From the voltammograms, the C_{sp} of the electrodes was determined using equation (5):

$$C_{sp} = \frac{2i}{Sm} \quad (5)$$

where i is the electric current, S is the scan rate and m is the weight of electrode.

From the GCD data (charge-discharge curve) recorded at a selected current density, the C_{sp} of the electrodes was determined using equation (6):

$$C_{sp} = \frac{2i}{\left(\frac{\Delta V}{\Delta t}\right)m} \quad (6)$$

where i is the discharge current, ΔV is the voltage and Δt is the discharge time [15-17]. The values of the specific power (P) and specific energy (E) were also calculated from the GCD data using the following equations (7) and (8), respectively:

$$P = \frac{Vi}{m} \quad (7)$$

$$E = \frac{Vit}{m} \quad (8)$$

where i is the discharge current, V is the voltage (excluding the iR drop occurring at the beginning of the discharge) and t is the time [18].

3. RESULTS AND DISCUSSION

3.1 Physical and electrical properties

Table 1 shows the weight (w), thickness (t), diameter (d) and density (ρ) of the GMs, CMs and ACMs, along with the electrical conductivity (σ) of the ACMs. Analysis of the ACM data reveals that the samples experienced 52.70% to 55.54% weight loss and 22.43% to 27.06% dimensional shrinkage after carbonization. These effects are due to the release of the non-carbon material and rearrangement of the carbon atoms during the carbonization and activation processes. A small difference between the weight loss and dimensional shrinkage percentages has been observed elsewhere [13,19] and is a major factor contributing to the small differences in the sample densities before and after carbonization. The

density of the ACMs is slightly higher compared to the density of the bamboo carbon electrode, 0.63 to 0.95 g cm⁻³ [20], and rubber wood sawdust carbon electrode, 0.63 to 0.85 g cm⁻³ [21]. The electrical conductivity of the ACMs seems to change slightly with the carbonization temperature, which corresponds to a small change in the densities of the ACMs. According to percolation theory and the granular model, the electrical conductivity of the carbon sample is proportional to its density [22].

Table 1. Weight, dimensions and density of the GMs, CMs and ACMs, and electrical conductivity of the ACMs.

Samples	w (g)	d (mm)	t (mm)	ρ (g cm ⁻³)	σ (S cm ⁻¹)
GM6	0.7351	2.19	20.15	1.053	-
GM7	0.7443	2.22	20.17	1.050	-
GM8	0.7283	2.18	20.12	1.051	-
CM6	0.3485	1.64	15.63	1.108	-
CM7	0.3295	1.62	15.39	1.094	-
CM8	0.3158	1.59	15.14	1.104	-
ACM6	0.3129	1.59	14.68	1.163	14.31
ACM7	0.3259	1.59	15.00	1.160	13.82
ACM8	0.3192	1.59	14.97	1.141	13.49

Figure 1 shows the XRD data of the ACM6, ACM7 and ACM8 specimens. These data show that all of the ACMs have a turbostratic structure, which implies that the building blocks of the ACMs are composed of graphitic-like microcrystallites that are randomly oriented and distributed throughout the samples [23-25]. All of the ACMs shows a similar diffraction pattern with two broad peaks at diffraction angles of 25° and 41.6°, corresponding to the (002) and (100) peaks, respectively. The intense peaks around 25.6° are due to the addition of CNT. From these peaks, the values of the structural parameters, such as the interlayer spacing, d_{002} and d_{100} , and microcrystallite dimensions, L_c (stack height) and L_a (stack width), were determined. The values of d_{002} and d_{100} were calculated using Bragg's equation ($n\lambda = 2d\sin\theta$, where $n = 1$, λ is the wave length (1.5406 Å) of the X-ray radiation and θ is the Bragg angle representing the position of the (002) and (100) diffraction peaks). The values of L_c , determined from the (002) peak, and L_a , determined from the (100) peak, were calculated using the Debye-Scherrer equation ($L_{c,a} = K\lambda/\beta_{c,a} \cos\theta$, where K is the shape factor equal to 0.89 and 1.84 for L_c and L_a , respectively, and $\beta_{c,a}$ is the full width at half maximum of the symmetrically shaped diffraction peaks).

The calculated values of the structural parameters are shown in Table 2. The change in the d_{002} and d_{001} values is very small and does not have a systematic trend to be correlated with the change of the carbonization temperature. However, the microcrystallite dimensions (L_c and L_a) in the ACMs seem to change significantly with carbonization temperature. These results could be further analyzed in terms of the ratios of L_c/d_{002} and L_c/L_a . The former ratio represents the mean number of planes in the microcrystallites (N_p), while the later ratio represents the relative density of edge and basal planes in the microcrystallites. The relative density of edge and basal planes is a measure of the edge orientation

of the microcrystallites. The values of N_p in Table 2 clearly indicate that increasing the carbonization temperature causes the microcrystallites in the ACMs to have a higher number of graphitic-like planes. The values of the latter ratio seem to decrease significantly with the increasing carbonization temperature, indicating that carbonization temperatures closer or equal to the activation temperature can lead to the generation of plate-like microcrystallites in the ACMs during the activation process. The values of this ratio for the carbon samples produced under other experimental conditions and using coffee endocarp precursor [8] for the supercapacitor electrodes have been reported to be within the range of 0.32 to 0.67 and are comparable with the L_c/L_a values listed in Table 2.

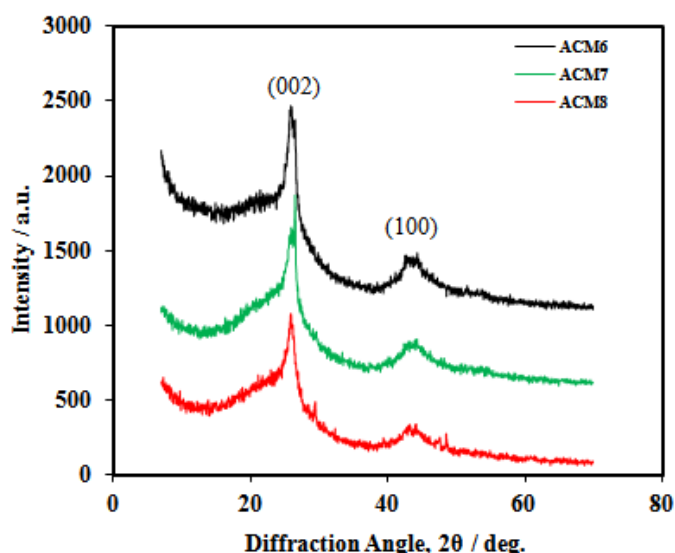


Figure 1. XRD patterns for the ACMs.

Table 2. Interlayer spacing and microcrystallite dimensions for the ACMs.

Samples	d_{002} (Å)	d_{100} (Å)	L_c (Å)	L_a (Å)	L_c/d_{002}	L_c/L_a
ACM6	3.5782	1.9895	9.81	13.20	2.742	0.743
ACM7	3.6137	2.0405	9.35	34.50	2.587	0.271
ACM8	3.5676	2.0667	12.45	57.17	3.489	0.218

The relationship between d_{002} , L_c and the BET surface area (S_{BET}) of the carbon material is given by $S_{BET} = 2 \times d_{002(carbon)} / (d_{002(graphite)} \times \rho_{(graphite)} \times L_c)$, where $d_{002(graphite)} = 0.3335 \text{ g cm}^{-3}$ and $\rho_{(graphite)} = 2.26 \text{ g cm}^{-3}$ [23]. There have been many reports that include the d_{002} and L_c data when considering the dependence of the supercapacitor C_{sp} on the BET surface area [8,26]. A model that quantitatively relates the C_{sp} and the surface area of the active material in the electrode has been developed by Emmenegger et al. (2003) [27]; recently, this model has been used to study carbon electrodes from EFB fibers, with reported values of d_{002} , L_c and the BET surface area in the ranges from 3.5320 to 3.6081 Å, 8.4329 to 19.2165 Å and 485 to 1125 $\text{m}^2 \text{ g}^{-1}$, respectively [23]. It will be

revealed in a later section that the surface area data collected in this study also change with the L_c values shown in Table 2.

For the FESEM investigation, the ACMs were fractured, and the FESEM micrographs of these fractured surfaces are shown in Figures 2 (a-c). These micrographs show the porous characteristics of the ACM6, ACM7 and ACM8 electrodes. The rough texture represents the grain boundary surfaces, while the smooth texture represents the fractured grain surfaces. The ACM8 electrode seems to have a larger grain size than the other electrodes, which is consistent with the dimensional data of microcrystallites listed in Table 2.

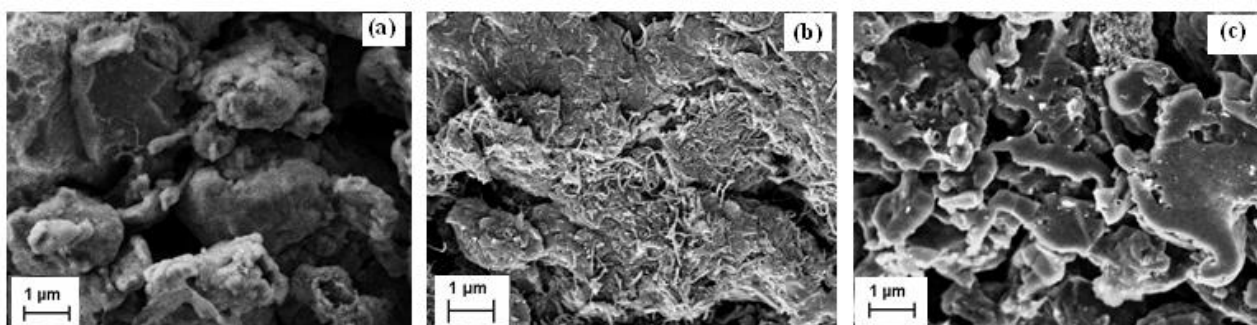


Figure 2. FESEM micrographs for (a) ACM6, (b) ACM7 and (c) ACM8.

Figure 3 demonstrates that all of the samples exhibit a typical I-type isotherm [28], indicating that all of the electrodes are microporous solids with low external and high internal surface areas. The rounded knee in the low relative pressure indicates that the samples possess a wide pore size distribution that varies from the micropore to mesopore range. The flat curve over a wide range of relative pressures indicates the existence of much more widely distributed and heterogeneous microporosity. The presence of the pronounced upward tail as the relative pressure approaches unity indicates that there are a larger amount of porous spaces and ink bottle pores shaped [29,30]. Although all of the curves show similar features, the adsorption-desorption capacity for ACM8 is significantly higher than for ACM6 and ACM7, indicating that the 800°C carbonization temperature is advantageous in converting CMs into ACMs.

Quantitative interpretation of the isotherms, shown in Figure 3, is listed in Table 3. The quantitative interpretation includes the BET surface area (S_{BET}), surface area of the mesopores (S_{Meso}) and micropores (S_{Micro}), volume of the mesopores (V_{Meso}) and micropores (V_{Micro}) and the average pore diameter (D_p). As revealed through these results, the preparation of the electrodes with a carbonization temperature equal to the activation temperature can play a significant role in promoting higher volumes of micropores relative to the mesopores and hence promote a higher surface area for electric-double layer formation in the electrodes, which is needed for enhancing the C_{sp} . This dependency on the carbonization temperature can also be highlighted by comparing the S_{Micro}/S_{Meso} ratios of ACMs; the S_{Meso}/S_{Micro} ratios for ACM8, ACM7 and ACM6 are 0.1358, 0.1468 and 0.1481, respectively. It should be noted that there have been many studies that consider the C_{sp} in terms of this ratio variation;

a recent report on bamboo-based activated carbon electrodes observed that the ratios of $S_{\text{Meso}}/S_{\text{Micro}}$ can vary from 0.09 to 0.45, corresponding to C_{sp} values from 55 to 67 F g⁻¹ at the current density of 1 mA cm⁻² [20].

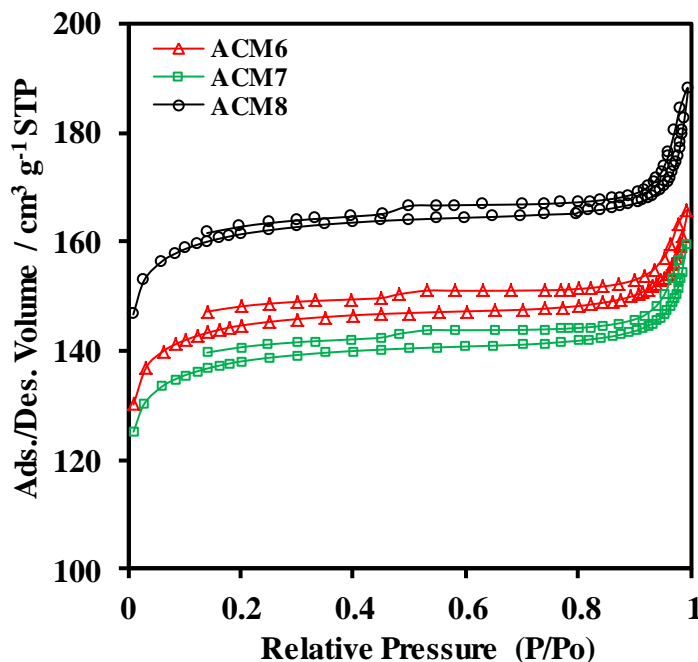


Figure 3. The adsorption-desorption capacity versus relative pressure for the ACMs.

Table 3. Porosity data for the ACMs.

Samples	ACM6	ACM7	ACM8
S_{BET} (m ² g ⁻¹)	434	415	485
S_{Meso} (m ² g ⁻¹)	56	53	58
S_{Micro} (m ² g ⁻¹)	378	361	427
V_{Meso} (cm ³ g ⁻¹)	0.0501	0.0492	0.0538
V_{Micro} (cm ³ g ⁻¹)	0.1988	0.1898	0.2241
D_p (nm)	2.2912	2.3019	2.2903

3.2 Electrochemical properties

3.2.1 Electrochemical impedance spectroscopy

The EIS data expressed as Nyquist plots over the frequency range of 10⁻¹ to 10⁶ Hz for the ACM based supercapacitor cells are given in Figure 4. This figure, particularly the inset, clearly shows the effects of changing the carbonization temperature on the small semicircle (first segment), Warburg diffusion line (second segment) and capacitive line (third segment). A relatively small semicircle in the high frequency region represents the dominant resistive nature of the supercapacitor system consisting

of electrode/electrolyte/current-collector. The beginning of the semicircle line (left-intercept of Z'' at the Z' axis) represents the resistance (R_s) of the electrolyte in contact with the current collector and electrode. The termination of the semicircle line (right-intercept of Z'' at the Z' axis) represents the internal resistance (R_p) of the electrode. The diameter of the semicircle ($R_p - R_s$) is equal to the ESR value. The values of R_s , R_p and ESR for all the cells determined from the data in Figure 4 are listed in Table 4. These results do not show any specific trend with respect to changing the carbonization temperature, but the magnitude of the ESR values are typical for carbon based supercapacitors. For example, Kim et al. (2006) have reported the ESR values of 0.134 to 1.149 Ω for the bamboo based activated carbon electrodes [20].

The second segment (straight line with a slope of approximately 45°) in the middle frequency region represents the combination of resistive and capacitive behaviors of the ions penetrating into the electrode pores. The length, slope and position of this segment appear to be affected by changes in the carbonization temperature. A steep slope corresponding to electrodes that efficiently allow ions to penetrate pores has been observed in another study on carbon electrodes from porous carbon powder [31].

The third segment (straight lines sharply increasing at the low-frequency region) represents the dominance of capacitive behavior from the formation of ionic and electronic charges of the electric double layer system at the micropore surfaces; at this frequency, the ions can more easily diffuse into the micropores [31-34]. The initiation point of this third segment line corresponds to the knee frequency (f_k), and its corresponding resistance (R_k) is given by Z'_k . The values of f_k and R_k are given in Table 4. These results seem to show that carbonization at 800°C may change the capacitive region to begin at a relatively higher frequency value with a lower resistance. The length of this straight line is shorter for the ACM8 cell compared to the other two cells; furthermore, the line for the ACM8 cell leans more towards the vertical Z'' axis, indicating that the ACM8 cell has a better capacitive performance. The values of the C_{sp} calculated from the EIS data using equation (1) are shown in Table 5 and reveal that this ACM8 cell has the highest C_{sp} .

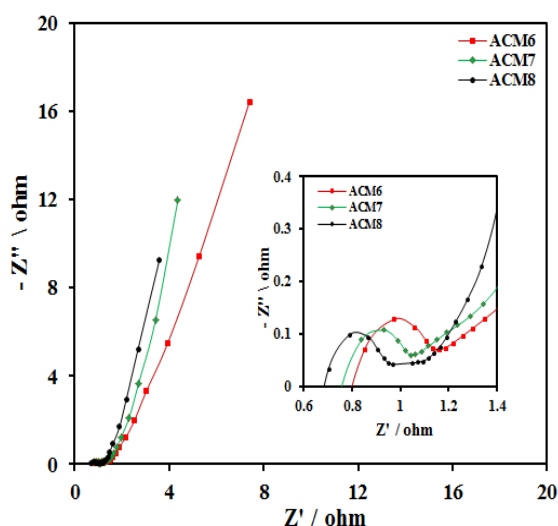


Figure 4. Nyquist plots for the ACM cells.

Table 4. The values of R_s , R_p , ESR, f_k and R_k for the ACM cells.

Cells	R_s (Ohm)	R_p (Ohm)	ESR (Ohm)	f_k (Hz)	R_k (Ohm)
ACM6	0.877	1.084	0.207	5	1.522
ACM7	0.749	1.064	0.315	10	1.344
ACM8	0.860	1.063	0.203	40	1.138

Figures 5 (a) and (b) show the specific, imaginary (C'') and real (C') capacitance portions of the ACM cells calculated using equations (1), (3) and (4) as a function of frequency. In Figure 5 (a), the C_{sp} strongly depends on the frequency below 1 Hz, particularly for the ACM8 cell, which shows a higher C_{sp} throughout the entire frequency region. A similar frequency dependency is also exhibited by the C' and C'' curves in Figure 5 (b). For the C'' curve, there is a peak frequency value (f_p). This frequency value is associated with the relaxation time constant, τ_o , which defines the boundary between the regions of capacitive and resistive behaviors for the supercapacitor. It is well known that higher power delivery corresponds to lower τ_o values.

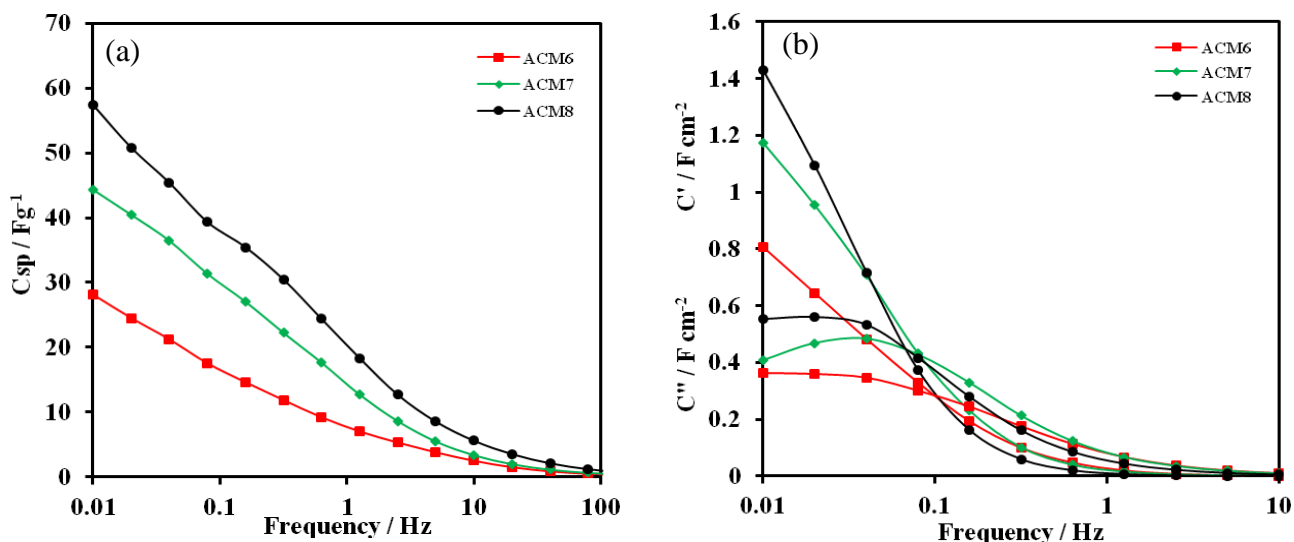


Figure 5. (a) Specific capacitance versus frequency, (b) Evolution of imaginary and real portions of capacitance for the ACM cells.

Based on the f_p values in Figure 5 (b), the value of τ_o was estimated using the equation $\tau_o = 1/f_p$, the results of which are 25.12 and 50.13 s for the ACM7 and ACM8 cells, respectively. The τ_o value for the ACM6 cell cannot be calculated because the peak lies below the detection limit of the instrument. These calculated τ_o values are within the same order of magnitude as that reported by Garcia-Gomes et al. (2010); 3.8 to 62 s for the CM electrodes based on another type of precursor [35].

Other investigations showed values of τ_0 in the range of 3 to 68 s for carbon electrodes prepared from micro/mesoporous carbon C(Mo₂C) [36].

3.2.2 Cyclic voltammetry

The supercapacitive properties of the ACM6, ACM7 and ACM8 cells were determined using cyclic voltammetry because this method provides valuable information on the charge-discharge behavior of the cells. The measurements were performed at room temperature within the potential range of 0 to 1 V and over a scan rate of 1 to 100 mVs⁻¹. Fig 6 (a) shows the measured cyclic voltammograms recorded at 1 mVs⁻¹ for the ACM6, ACM7 and ACM8 cells. The shape of the voltammograms for all the cells is rectangular, representing a typical voltammogram for electric double-layer capacitance [37]. Comparing the voltammograms of the ACM6, ACM7 and ACM8 cells in Figure 6 (a), it can be observed that the ACM8 cell has a broader voltammogram area. These results indicate that the ACM8 cell has a better cycle reversibility and higher electric double-layer capacitance stability during the charge and discharge processes compared with the other cells. Ultimately, these effects correspond to a higher C_{sp} for the ACM8 cell. The C_{sp} of the ACM6, ACM7, and ACM8 electrodes were calculated using the equation (5) from the voltammograms (Figure 6) recorded with a scan rate of 1 mVs⁻¹. These results are shown in Table 5 and are in good agreement with the obtained EIS results.

It is also observed that the voltammograms (scan rate of 1 mVs⁻¹) in Figure 6 (a) do not have any peaks, which indicates that the supercapacitive behavior is free from redox reactions or is purely based on the electrostatic mechanism. It was also found that this behavior was exhibited by all of the cells when the scan rate was varied up to 100 mVs⁻¹. To observe such a supercapacitive behavior over a range of scan rate, Figure 6 (b) shows the voltammograms for the ACM8 cell at five different scan rates (1, 5, 25, 50, and 100 mVs⁻¹). Figure 6 (b) demonstrates that the current response increased with the scan rate. Furthermore, as the scan rate increased above 5 mVs⁻¹, the voltammograms 'window' tended to tilt toward the vertical axis, thereby becoming a quasi-rectangle. This result indicates the dominance of the double layer formation in the energy storage process at lower scan rates.

Figure 6 (c) shows the C_{sp} values determined using equation (5) and the voltammograms obtained at different scan rates for all the ACM cells. All cells show a common trend of decreasing C_{sp} values against an increasing scan rate. It is well known that for very low scan rates, the C_{sp} values are higher because the ions have a much longer time to penetrate and reside in all the available electrode pores and form electric double layers, which are needed to generate higher capacitance. Despite this common trend, the ACM8 cell displays higher C_{sp} values throughout the whole scan region, clearly indicating its superiority over the other two cells. This result is in agreement with the EIS results discussed in the preceding section. In the scan rate region above 5 mVs⁻¹, the C_{sp} for the ACM8 seemed to decrease faster than that for the ACM6 and ACM7 cells as the scan rate increased; these results are evidence of the increasing diffusion resistance towards the ionic motion into the electrode pores, which is not linear with respect to the change in the carbonization temperature during electrode preparation. This non-linear effect has also been observed in investigations assessing the dependence of electrode C_{sp} on the quantity of binder used during electrode preparation [38].

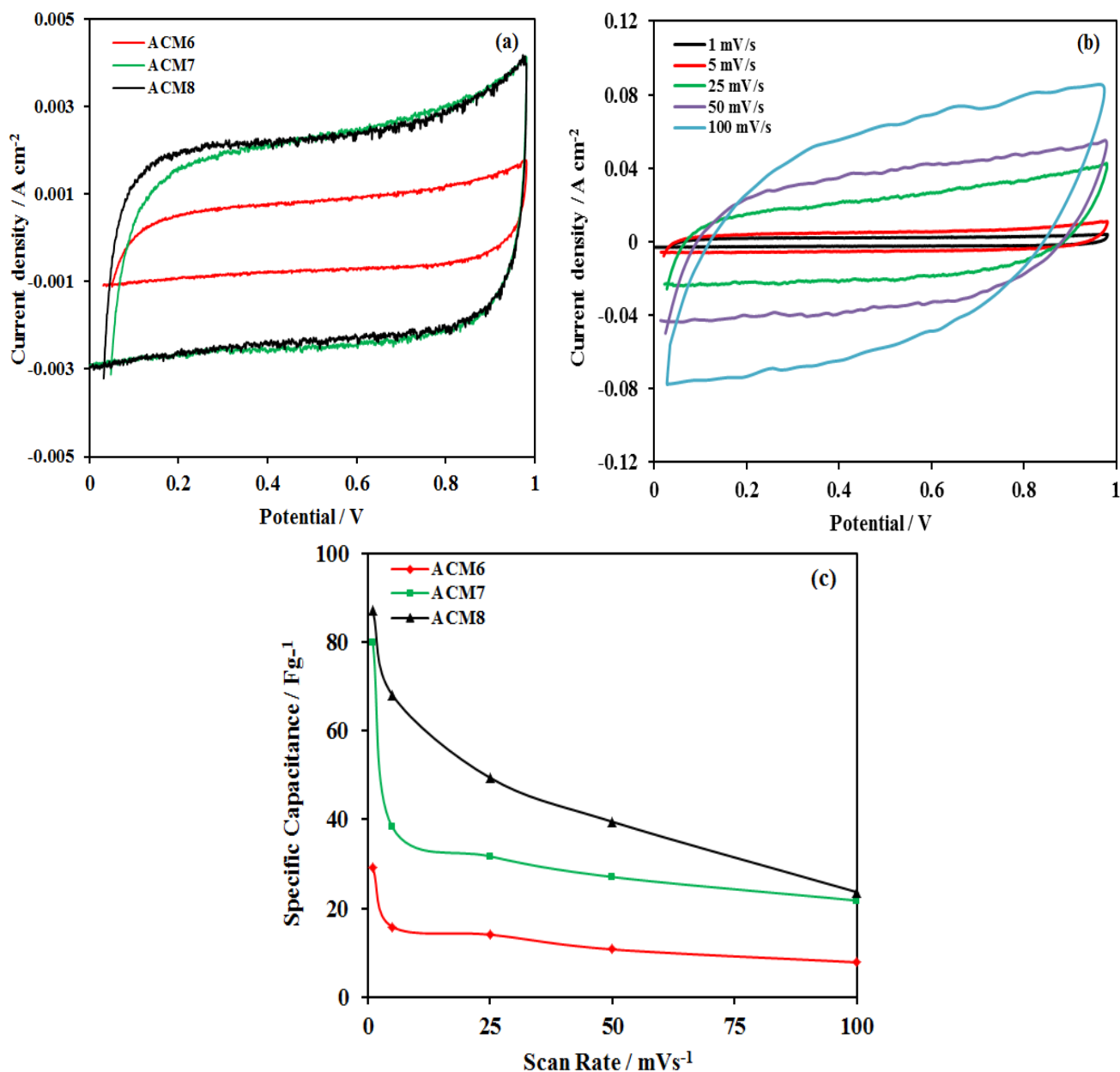


Figure 6. (a) CV curves at the scan rate 1 mVs⁻¹ for the ACM cells, (b) CV curves with various scan rates for the ACM8 cell, and (c) Specific capacitance versus scan rate for the ACM cells.

3.2.3 Galvanostatic charge-discharge

The GCD curves for all the ACM cells recorded in the potential range of 0 – 1 V and at a current density of 10 mA cm⁻² are shown in Figure 7. As seen in this figure, all the cells show a similar symmetrical triangular curve with a nearly linear variation of voltage as a function of time during charge and discharge. This type of curve is typical for carbon-based supercapacitors, and the data shows that all the three cells have a good supercapacitive performance. However, despite having a

similar shape, the curves for the ACM7 and ACM8 cells, particularly the latter, show significantly higher charge and discharge times, as shown in Figure 7; these observations indicate that a higher number of electrons and electrolyte ions are participating in the charge and discharge processes of these electrodes compared to the ACM6 electrode. This is further evidence supporting the results obtained by the EIS and CV methods that determined carbonization temperatures closer or equal to the activation temperature can produce better electrodes for supercapacitor application. Put more directly, the carbonization temperature of 600°C is too low to be compatible with the 800°C activation temperature used during electrode preparation.

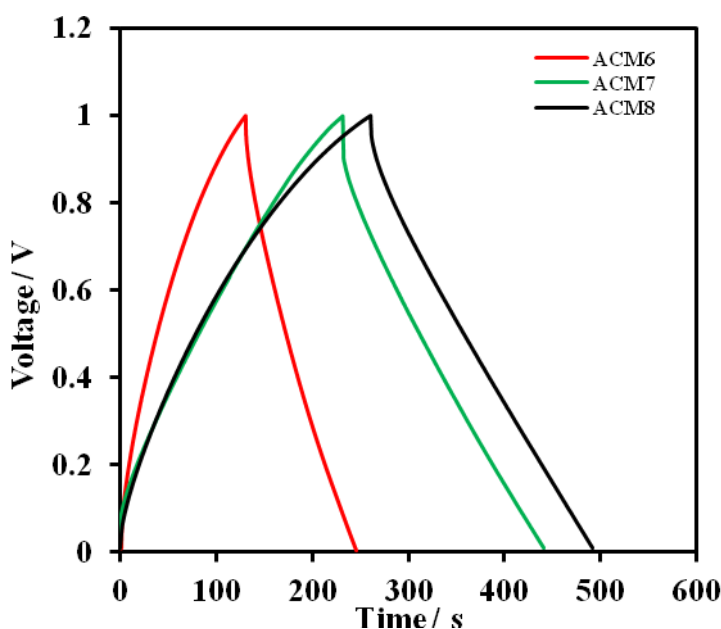


Figure 7. GCD curves for the ACM cells.

As revealed in Figure 7, a sharp drop in the initial voltage upon discharge is evident and results from diffusion-limited mobility of the electrolyte ions in the electrode pores. This limitation is associated with the equivalent series resistance (ESR) of the supercapacitor cells. The ESR value is calculated from this voltage drop using the equation $ESR = iR_{\text{drop}}/2i$. The ESR values for the ACM6, ACM7 and ACM8 cells are 2.615, 4.852 and 2.437 Ohm, respectively, clearly indicating that the ACM8 cell offers the lowest ESR value. These ESR values are comparable with the results of other researchers who observed ESR values ranging from 1.17 to 3.69 Ohm for carbon electrode mixtures composed of activated carbon, graphite and polytetrafluoroethylene (PTFE) [39] and from 9.7 to 16.7 Ohm for carbon electrodes derived from activated carbon powder [40]. These literature ESR values derived from the GCD data are higher than those derived from the EIS data. This trend is also observed in the ESR results reported here.

The C_{sp} values of the supercapacitor cells based on ACM electrodes were calculated from the data in Figure 7 using equation (6) and are shown in Table 5. As expected, these values follow the trend of C_{sp} values calculated from the EIS and CV data, i.e., showing a good trend of overall change

in magnitude with respect to the change in carbonization temperature. For comparison, some of the C_{sp} values reported in the literature for other types of carbon electrodes used in supercapacitors are also included in Table 5.

Table 5. Specific capacitance (C_{sp}) for the ACMs cells ($x = \text{EIS}$, $y = \text{GCD}$, $z = \text{CV}$).

Cells	$^x C_{sp}$ (Fg^{-1})	$^y C_{sp}$ (Fg^{-1})	$^z C_{sp}$ (Fg^{-1})
ACM6	28	55	27
ACM7	44	77	78
ACM8	61	85	80
Ref. [2]	-	235-319	226-339
Ref. [8]	38-90	2-176	-
Ref. [9]	-	-	244-311
Ref. [28]	-	135-329	228-358
Ref. [29]	-	230-300	-

3.2.4 Specific energy and power

The specific power and specific energy of the ACM cells were calculated from the GCD curves (Figure 7) using equations (7) and (8), respectively [41]. The results are shown as Ragone plots in Figure 8, which indicate there is a correlation between the specific power and specific energy of the supercapacitor.

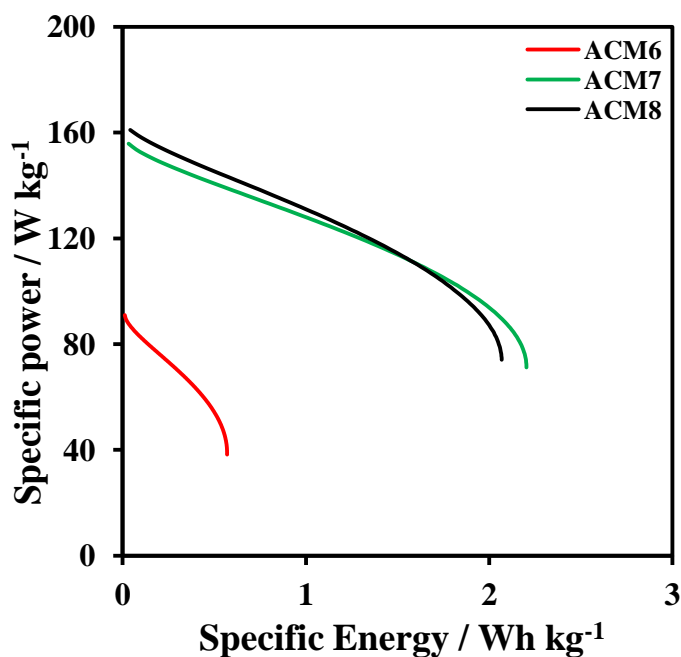


Figure 8. Ragone plots for the ACM cells.

The specific power linearly decreases with increasing specific energy for all the cells, which means that less energy is released at higher power output. However, as shown in Figure 8, the power-energy relationship for the ACM7 and ACM8 cells seem to be much better than that of the ACM6 cell; again demonstrating that the carbonization temperature closer or equal to the activation temperature may help producing better performance of the ACM electrodes for supercapacitor application (also shown by the EIS and CV data in the preceding sections). The maximum specific energy and specific power determined were 2.2 Wh kg^{-1} and 156 W kg^{-1} , respectively, for the ACM7 cells and 2.1 Wh kg^{-1} and 161 W kg^{-1} , respectively, for the ACM8 cells. These results are comparable to the typical ranges of specific energy and specific power values for supercapacitor electrodes derived from other types of biomass precursors, i.e., cherry stones fell within the range of 3.5 to 5 Wh kg^{-1} and 700 to 1900 W kg^{-1} , respectively [29]. A similar range of specific energy and specific power values was observed between 2.6 to 3.3 Wh kg^{-1} and 580 to 620 W kg^{-1} , respectively, for carbon electrodes prepared from rubberwood sawdust precursor [29] and between 0.5 to 3.5 Wh kg^{-1} and 150 to 160 W kg^{-1} , respectively, for carbon electrodes from oil palm empty fruit bunch fibers precursor [11].

4. CONCLUSION

GMs consisting of SACG EFB fibers (95% by weight), CNTs (5%) and KOH (5%) were heated to 600 , 700 and 800°C carbonization temperatures (CTs), respectively, to produce CM6, CM7 and CM8. These CMs were activated by CO_2 at 800°C to produce ACM6, ACM7 and ACM8, which were used as electrodes in supercapacitor cells. We observed that the changes in the density, electrical conductivity, porosity, microstructure and structure of the ACMs due to the change in the CT notably affected the electrochemical behaviors of the supercapacitor cells. Characterization by EIS, CV and GCD methods consistently found that the cells using the ACMs from the CMs (CT = 700 , 800°C) exhibit better specific capacitance, specific energy and specific power than that from the CM (CT = 600°C). These results lead to the conclusive recommendation that the CT value should be closer or equal to the activation temperature for the production of higher quality ACM electrodes from CMs.

ACKNOWLEDGMENTS

We acknowledge grants from the Universiti Kebangsaan Malaysia (UKM-GUP-216-2011, UKM-DLP-2012-022, and UKM-DLP-2012-023), and the support of CRIM (Centre for Research and Innovation Management). The authors also thank Mr. Saini Sain for helping with the laboratory work.

References

1. Y. Liu, Z. Hu, K. Xu, X. Zheng and Q. Gao, *Acta Phys. Chim. Sin.*, 24(7) (2008) 1143.
2. B. Xu, Y. Chen, G. Wei, G. Cao, H. Zhang and Y. Yang, *Mater. Chem. Phys.*, 124 (2010) 504.
3. P.L. Taberna, G.C. Chevallier, P. Simon, D. Plee and T. Aubert, *Mater. Res. Bull.*, 41 (2006) 478.

4. Q.Y. Li, Z.S. Li, L. Lin, X.Y. Wang, Y.F. Wang, C.H. Zhang and H.Q. Wang, *Chem. Eng. J.*, 156 (2010) 500.
5. J.M. Ko and K.M. Kim, *Mater. Chem. Phys.*, 114 (2009) 837.
6. L. Chunlan, X. Shaoping, G. Yixiong, L. Shuqin and L. Changhou, *Carbon*, 43 (2005) 2295.
7. C. Grini, *Bioresour. Technol.*, 97 (2006) 1061.
8. J.M. Valente Nabais, J.G. Teixeira and I. Almeida, *Bioresour. Technol.*, 102 (2011) 2781.
9. X. Li, W. Xing, S. Zhuo, J. Zhou, F. Li, SZ. Qiao and G.Q. Lu, *Bioresour. Technol.*, 102 (2011) 1118.
10. Awitdrus, M. Deraman, I.A. Talib, R. Farma, R. Omar, M.M. Ishak, N.H. Basri and B.N.M. Dolah, *Adv. Mater. Res.*, 501 (2012) 13.
11. R. Farma, M. Deraman, R. Omar, Awitdrus, M.M. Ishak, E. Taer and I.A. Talib, *AIP Proceeding*, 1415 (2011) 180.
12. M. Deraman, M.M. Ishak, R. Farma, Awitdrus, E. Taer, I.A. Talib and R. Omar, *AIP Proceeding*, 1415 (2011) 175.
13. M. Deraman, R. Omar, S. Zakaria, I.R. Mustapa, M. Talib, N. Alias and R. Jaafar, *J. Mater. Sci.*, 37 (2002) 3329.
14. C. Portet, O.L. Taberna, P. Simon, E. Flahaut and C. Laberty Robert, *Electrochim. Acta*, 50 (2005) 4174.
15. M. Beidaghi, W. Chen and C. Wang, *J. Power Sources*, 196 (2011) 2403.
16. K.C. Tsay, L. Zhang and J. Zhang, *Electrochim. Acta*, 60 (2012) 428.
17. A.B. Fuertes, G. Lota, T.A. Centeno and E. Frackowiak, *Electrochim. Acta*, 50 (2005) 2799.
18. S.R.S. Prabaharan, R. Vimala and Z. Zainal, *J. Power Sources*, 161 (2006) 730.
19. M. Deraman, S. Zakaria, R. Omar and A.A. Aziz, *Jpn. J. Appl. Phys.*, 39 (2000) L1236.
20. Y.J. Kim, B-J Lee, H. Suezaki, T. Chino, Y. Abe, T. Yanagiura, K.C. Park, M. Endo, *Carbon*, 44 (2006) 1592.
21. E. Taer, M. Deraman, I.A. Talib, A.A. Umar, M. Oyama and R.M. Yunus, *Curr. Appl Phys.*, 10 (2013) 1071.
22. M. Deraman, *J. Phys D: Appl. Phys.*, 27 (1994) 1060.
23. Awitdrus, M. Deraman, I.A. Talib, R. Omar, M.H. Jumali, E. Taer and M.M. Saman, *Sains Malaysiana*, 39 (2010) 83.
24. A.R. Coutinho, J.D. Rocha and C.A. Luengo, *Fuel Process. Technol.*, 67 (2000) 93.
25. M. Deraman, S.K.M. Saat, M.M. Ishak, Awitdrus, E. Taer, I.A. Talib, R. Omar and M.H. Jumali, *AIP Proceeding*, 1284 (2010) 179.
26. D. Qu, *J. Power Sources*, 109 (2002) 403.
27. Ch. Emmenegger, Ph. Mauron, P. Sudan, P. Wenger, V. Herman, R. Gallay and A. Zuttel, *J. Power Sources*, 124 (2003) 321.
28. M. Khalfaoui, S. Knani, M.A. Hachicha and A. Ben Lamine, *J. Colloid Interface Sci.*, 263 (2003) 350.
29. E. Taer, M. Deraman, I.A. Talib, S.A. Hashmi and A.A. Umar, *Electrochim. Acta*, 56 (2011) 10217.
30. F-C. Wu, R-L. Tseng, C-C. Hu, C-C. Wang, *J. Power Sources*, 159 (2006) 1532.
31. W.C. Chen, T.C. Wen and H. Teng, *Electrochim. Acta*, 48 (2003) 641.
32. F. Rafik, H. Guolous, R. Gallay, A. Crausaz and A. Berthon, *J. Power Source*, 165 (2007) 928.
33. Y.R. Nian and H. Teng, *J. Electroanal. Chem.*, 540 (2003) 119.
34. J. Gamby, P.L. Taberna, P. Simon, J.F. Fauvarque and M. Chesneau, *J. Power Sources*, 101 (2001) 109.
35. A. Garcia-Gomez, P. Miles, T.A. Centeno and J.M. Rojo, *Electrochim. Acta*, 55 (2010) 8539.
36. T. Thomberg, A. Janes and E. Lust, *Electrochim. Acta*, 55 (2010) 3138.
37. A.I. Inamdar, Y.S. Kim, S.M. Pawar, J.H. Kim, H. Im, H. Kim, *J. Power Sources*, 196 (2011) 2393.

38. J. Yan, T. Wei, B. Shao, Z. Fan, W. Qian, M. Zhang, F. Wei, *Carbon*, 48 (2010) 487.
39. H. Yu, J. Wu, L. Fan, K. Xu, X. Zhong, Y. Lin and J. Lin, *Electrochim. Acta*, 56 (2011) 6881.
40. K.M. Kim, J.W. Hur, S. I. Jung and A.S. Kang, *Electrochim. Acta*, 50 (2004) 863.
41. M. Olivares-Marin, J.A. Fernandez, M.J. Lazaro, C. Fernandez-Gonzalez, A. Macias-Garcia, V. Gomez-Serrano, F. Stoeckli and T.A. Centeno, *Mater. Chem. Phys.*, 114 (2009) 323.

© 2013 by ESG (www.electrochemsci.org)